applied sciences

MDPI

Article

# Impact of Polar Environmental Factors on Upward Laser Energy Transmission

**Zhe Wu, Wenyong Guo, Xiaofeng Li, Li Yu, Shihao Zhu, Xin Xiong, Zicheng Shu and Jianggui Han ***

College of Power Engineering, Naval University of Engineering, Wuhan 430033, China; 1920191013@nue.edu.cn (Z.W.); guowy202@163.com (W.G.); 2120213016@nue.edu.cn (X.L.); 0908042009@nue.edu.cn (L.Y.); x24182402@nue.edu.cn (S.Z.); 1010021048@nue.edu.cn (X.X.); x25182407@nue.edu.cn (Z.S.)

* Correspondence: 0908041062@nue.edu.cn

**Abstract**

Underwater laser detection and communication in polar regions have attracted increasing research interest. The stochastic roughness of the water–ice interface causes the broadening of the incident beam angle and spatial energy uncertainty, posing critical challenges for cross-medium optical transmission. This study presents a theoretical model that couples seawater volumetric scattering attenuation with rough-interface effects in upward laser transmission. The water–ice interface is discretized using Beckmann–Gaussian microfacet geometry. From this, the analytical relationship between local surface normal distributions and Fresnel reflection/transmission coefficients is derived. This enables the quantitative characterization of the process by which interface roughness modulates optical transmission. A full-link energy normalization framework is established. It encompasses normalized seawater-segment power, interface transmission efficiency, and normalized sub-ice received power. Monte Carlo photon tracing is used to simulate scattering in polar seawater and stochastic coupling at the rough interface. The results are experimentally validated. The key findings are as follows: Rising seawater temperature increases absorption but reduces scattering resulting in enhanced overall attenuation and degraded energy transfer efficiency. Interface roughness broadens the local angle-of-incidence distribution, and beyond 30°, energy transfer efficiency drops markedly. As propagation distance increases, normalized received power decreases, the beam spot diameter increases, and collimation quality deteriorates. The simulation results show strong agreement with the experimental measurements. These findings provide theoretical support for sub-ice laser signal acquisition and polarization modulation in polar environments, offering practical guidance for system design in underwater optical communication applications.

**Keywords:** water–ice interface; gaussian laser; normalized received power; Monte Carlo method

Check for updates

Academic Editor: Luis Cerdan

Received: 4 June 2026
Revised: 23 July 2026
Accepted: 24 July 2026
Published: 4 August 2026

**Copyright:** © 2026 by the authors. Licensee MDPI, Basel, Switzerland. This article is an open access article distributed under the terms and conditions of the Creative Commons Attribution (CC BY) license.

## 1. Introduction

The Arctic, often referred to as "the last treasure trove of the Earth," constitutes a strategic corridor connecting Asia, Europe, and the Americas, and its political, economic, scientific, and military values have become increasingly prominent. Although Arctic sea ice accounts for only a small fraction of the total ocean surface area, it plays a pivotal role in regulating the global climate system, mediating heat and gas exchange, modulating ocean structure, and governing polar ecosystem dynamics [1]. China's approach to the Arctic adheres to the principle of science-led engagement, with emphasis on environmental

protection, advocacy for rational resource utilization, promotion of rule-of-law governance, and commitment to international cooperation, while striving to uphold a peaceful, secure, and stable Arctic order [2]. Against the backdrop of the national strategic orientation of "expanding into the polar regions and maintaining an oceanic presence," research into laser propagation through aqueous media and solid-state interfaces has grown substantially in recent years.

Technological advances in laser systems have rendered the exploration and utilization of polar underwater resources increasingly feasible. This approach is particularly attractive for detection tasks in polar seas. By providing high spatial resolution and precise directional illumination, laser systems overcome many traditional sensing limitations in these challenging environments. The potential for high-rate optical links further enhances the appeal of laser technology in polar regions. However, as the beam traverses seawater and sea ice, it undergoes severe attenuation due to particle absorption and scattering, compounded by complex refraction and reflection at non-ideal water–ice interfaces characterized by random roughness and structural pits. The accurate modeling of these propagation characteristics across both aquatic and solid media is therefore essential. Recently, numerical methods—particularly Monte Carlo (MC) techniques—have become the standard for analyzing such cross-medium laser transmission [3]. Egerev S. V. et al. mainly investigated the statistical characteristics of laser-induced cavitation and its modeling by using the Monte Carlo method. When short laser pulses interact with liquids or biological tissue media, localized energy deposition can induce rapid heating, vaporization, and abrupt pressure variations, thereby triggering the formation of cavitation bubbles. To describe this complex process, the authors introduced a Monte Carlo algorithm to perform stochastic simulations of potential nucleation events, cavitation threshold distributions, and bubble formation probabilities within the laser-irradiated region, and compared the simulation results with experimental observations [4]. According to the study by He J. H. et al., variations in the concentration of underwater media significantly affect the transmission characteristics of laser polarization. During underwater propagation, laser beams are subject to absorption and scattering caused by suspended particles, impurities, and dissolved substances in the medium, thereby influencing the stability and accuracy of laser detection, communication, and imaging systems. In general, higher concentrations of underwater media lead to poorer laser polarization transmission performance, as reflected by reduced transmitted light intensity, decreased degree of polarization, and weakened polarization stability. Therefore, in underwater laser applications, the influence of medium concentration on polarization transmission should be fully considered, and laser parameters, polarization modes, and detection models should be optimized to improve transmission performance in complex underwater environments [5]. He et al. integrated Mie scattering theory with the Monte Carlo (MC) method to simulate the propagation of a 520 nm Gaussian beam in seawater. Specifically, they enhanced the MC algorithm through refined photon sampling, coordinate updates, and weight corrections, using Mie theory to derive precise seawater optical parameters. Their numerical analysis further shows how suspended-sediment properties and initial beam divergence govern underwater laser behavior [6]. In related work, Guo et al. developed an MC model for seawater with suspended particulates. They derived a fitted relationship among maximum transmission depth, minimum initial photon number, and particle concentration, thereby significantly improving simulation efficiency and accuracy [7]. Ren et al. integrated Mie scattering and a bidirectional reflectance distribution function (BRDF) into an improved MC (IMC) framework to construct a full-link underwater imaging model; by optimizing gated reception to suppress backscattering, they achieved experimental validation with an error below 30% [8]. Yu et al. built an underwater laser transmission model based on the MC algorithm. They investigated how

different seawater types, attenuation coefficients, and receiver aperture sizes affect power attenuation and effective transmission distance [9]. Gao analyzed the full optical link of a laser beam propagating from the atmosphere through the air–sea interface to seawater and studied the effects of particle properties, laser wavelength, and wind speed on the scattering/extinction coefficients and received power, demonstrating that seawater attenuation is the dominant factor limiting laser transmission in cross-medium systems and thereby providing theoretical guidance for system design [10]. Huang et al. used airborne lidar and a semi-analytical MC approach to establish a cross-medium underwater laser transmission model capable of simulating the entire echo signal chain; they analyzed the echo characteristics of underwater targets of different shapes (planar, conical, spherical, and spheroidal) at various depths, examined the impact of multiple scattering on echo energy, and evaluated the maximum detectable depth, full width at half maximum (FWHM) variation, and backscattered signal-to-noise ratio (SNR) for different targets, offering valuable insight for cross-interface propagation in seawater–sea ice scenarios [11]. In the literature, the rough ice–water interface is described based on Beckmann's classical rough-surface scattering theory, in which a rough surface is represented as a random height function and statistically characterized by RMS height, surface slope, and local normal distribution. Under the microfacet approximation, the interface is treated as an ensemble of small planar facets with different orientations, so incident photons encounter different local incidence angles and Fresnel reflection/transmission conditions. For Gaussian height or slope statistics, the microfacet slopes can be represented by a Beckmann–Gaussian distribution [12]. Zhang Y et al. combined MC simulation with the T-matrix method to study the propagation of polarized pulsed laser beams in turbid underwater environments with sand and algae as representative scatterers; they analyzed the impact of particle shape, composition, and turbidity on backscattered energy, polarization, and temporal pulse characteristics, showing that circular polarization is more robust against depolarization, flattened particles enhance backscattering, elongated particles favor forward scattering, and complex, absorbing algae induce stronger depolarization [13]. Chen Hui et al. applied fractal geometry to the study of engineering rough surfaces, simulating rough surface morphology using two approaches—the random midpoint displacement method and the Weierstrass–Mandelbrot (W-M) function—and demonstrated that the fractal dimension D and the characteristic scale A are more stable descriptors than conventional roughness parameters. They further established that a complete characterization of rough surfaces requires the simultaneous use of both fractal and statistical descriptors [14]. Welton compared two approximation methods for surface slope estimation, showing that the stochastic rough-surface slope approximation is consistent with the more comprehensive differential-operator approximation, which is applicable to all backscattering and specular scattering geometries, and that it achieves accuracy comparable to the source beam width [15]. Zhao M. W et al., motivated by the need for precise scattering analysis of ultra-smooth surfaces in high-precision optical systems, proposed a Generalized Beckmann–Kirchhoff (GBK) model. Through a comparative analysis of the Modified Beckmann–Kirchhoff (MBK) model and the Harvey–Shack (HS) model, they identified that the MBK model is capable of extracting the Power Spectral Density (PSD) function expression, which is subsequently incorporated into the MBK framework to formulate the GBK model [16,17]. Temperature is another important factor influencing laser propagation in polar environments. Changes in temperature can modify the thermal motion of seawater molecules and the surface microstructure of sea ice, thereby affecting the optical path, refraction angle, and refractive index, and consequently altering the Fresnel energy partitioning at the water–ice interface. Quan et al.'s empirical equation for the refractive index of seawater shows that the effect of temperature is manifested as a significant negative temperature coefficient [18]. Perovich and colleagues argue that sea ice

does not possess a single intrinsic refractive index; instead, its effective refractive index is governed by the volume fractions of its individual constituents. As temperature decreases, brine inclusions contract and the relative proportion of air bubbles increases, causing the effective refractive index to decrease and approach that of pure ice. Conversely, when temperature increases, the effective refractive index also increases [19].

Existing studies have predominantly focused on laser absorption in low-latitude water bodies, while systematic investigations of cross-medium laser transmission across water–ice interfaces at high latitudes remain scarce. In this work, a theoretical framework for upward laser transmission that integrates rough-interface coupling with full-link energy distribution is established. In contrast to conventional planar-interface assumptions, the Beckmann–Gaussian microfacet statistical approach is introduced for water–ice interface modeling. By performing statistical averaging over the randomly oriented local surface normals at the interface, an analytical method is developed to relate azimuthal randomness to surface roughness and to the Fresnel reflection and transmission coefficients, enabling the quantitative characterization of the extrema of the optical energy distribution at the interface. A normalized power representation framework is further defined, encompassing seawater volumetric scattering attenuation, interfacial energy coupling, and intra-sea-ice transmission, thereby realizing a complete energy transfer model for water–ice cross-medium propagation. The coupled modulation mechanisms of ambient temperature, transmission distance, and interface roughness on upward laser energy efficiency are systematically analyzed, yielding a nonlinear description of the angle-of-incidence broadening effect induced by rough interfaces on cross-medium transmission efficiency.

## 2. Theoretical Background

### *2.1. Upward Laser Transmission in Polar Seawater–Sea Ice*

In this study, the upward laser transmission process in high-latitude underwater environments is investigated under the following scene configuration. A right-handed Cartesian coordinate system is established with the origin located at the lower surface of the sea ice: the XOY plane coincides with the ice–water interface, and the Z-axis is directed downward. The seawater region satisfies $Z > 0$, and the lower surface of the sea ice satisfies $Z = 0$. The laser source is positioned at depth Zs beneath the interface, and the laser beam propagates in the negative Z-direction until it reaches the water–ice interface.

Given the optical complexity of the sub-ice polar seawater environment, this study proceeds as follows. First, a fundamental physical model is established, comprising a Gaussian beam propagation model, a seawater absorption–scattering model, and a Mie scattering approximation. The microstructural geometry of the rough water–ice interface is further refined through the construction of a microfacet statistical averaging model, which enables explicit microscopic characterization of the optical properties of the water–ice interface and provides an analytical quantification of the energy partitioning between refracted and reflected laser components. Second, on the basis of the application scenario, the attenuation model, and the theoretical framework governing energy distribution at the rough interface, we unify the underwater laser propagation process and the cross-medium transmission process at the water–ice interface into an integrated laser transmission model tailored to high-latitude sea-ice environments. Finally, a Monte Carlo algorithm is employed to trace photon trajectories and energy distribution throughout the propagation medium, with quantitative characterization performed using metrics including the normalized power at the interface, the normalized power transmitted into the sea ice, and the interface transmission efficiency.

Based on the observational data and summary of optical properties for polar under-ice seawater and sea ice, as reported by Perovich (1996–2000) for a blue-green laser at a

wavelength of 532 nm (specifically highlighting the 523–532 nm band) [19–21], this study adopts these parameters as the modeling baseline. The specific optical coefficients used in our simulations are summarized in Table 1.

**Table 1.** Optical parameters of polar seawater and sea ice used in the simulation (adapted from Perovich).

| Symbol | a/m$^{-1}$ | b/m$^{-1}$ | c/m$^{-1}$ | $\omega_0$/m$^{-1}$ | g | n |
|---|---|---|---|---|---|---|
| Physical quantity | Absorption coefficient | Scattering coefficient | Extinction coefficient | Single-scattering albedo | Asymmetry parameter | Refractive index |
| Natural waters | 0.035 | 0.057 | 0.092 | 0.71 | 0.95 | 1.342 |
| Natural sea ice | 0.15 | 2.00 | 2.15 | 0.94 | 0.90 | 1.295 |

When employing cross-medium uplink laser transmission for detection in polar environments, the inherent optical properties of seawater and sea ice differ significantly, and seawater at different latitudes [10] as well as sea ice from different years exert varying degrees of influence on underwater laser propagation. In natural polar waters, seawater is typically characterized by high clarity, with the dominant impurities comprising a limited amount of suspended particulates and organic matter, together with abundant high-salinity brine and ice crystals. Suspended particles are mainly composed of algae, phytoplankton, biogenic debris, and bubbles. These constituents generally exhibit a vertically stratified distribution, with lower concentrations near the surface and higher concentrations toward the bottom [16]. Since this study focuses on underwater laser transmission characteristics at depths within 2 m, the dominant factors governing propagation are the high-salinity brine and ice-crystal structures, which substantially modulate the absorption and scattering coefficients of the laser beam. At the water–ice interface, the incident light undergoes partial reflection back into the seawater, while the refracted component penetrates into the sea ice; however, the surface roughness and topographic irregularities of the sea ice critically alter the incident angle, effective power density, and transmission characteristics of the light entering the ice matrix [17]. A schematic diagram of the underwater laser uplink transmission system model is shown in Figure 1.

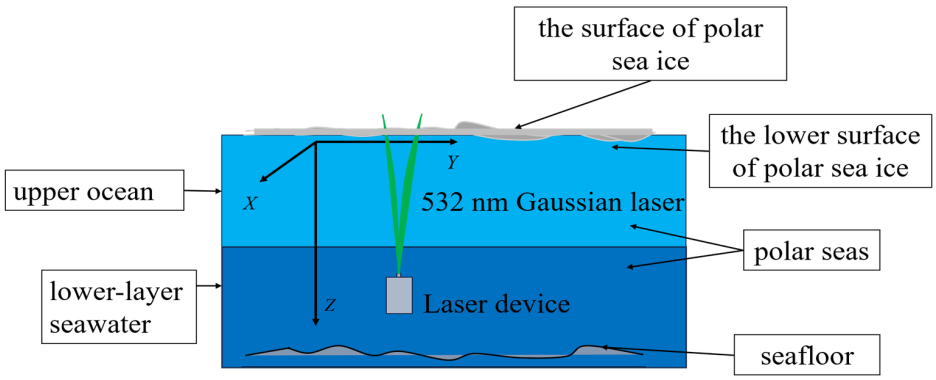


**Figure 1.** Underwater uplink laser transmission system model.

### 2.2. Gaussian Beam Model

The underwater laser source is modeled as a Gaussian beam propagating upward along the $z$-axis. In cylindrical coordinates, the electric field amplitude distribution takes the following form:

$$E(r, z_s) = \frac{E_0 \omega_0}{\omega(z_s)} \exp\left[\frac{-r^2}{\omega^2(z_s)}\right] \exp\left\{-\mathrm{i}\left\{k\left[\frac{r^2}{2R(z_s) + z_s}\right] - \xi\right\}\right\} \quad (1)$$

where $E_0$ denotes the maximum electric field amplitude at the beam waist center; $\omega_0$ is the initial beam waist radius; $\omega(z)$ and $R(z)$ are the beam width and the radius of curvature of the phase front at propagation distance Z, respectively; k is the wavenumber in the medium; and $\xi$ is the phase factor [20].

The intensity distribution at the emission plane satisfies:

$$I(r, z_s) = I_0 \exp\left(-\frac{2r^2}{\omega_0^2}\right) \tag{2}$$

where is the on-axis peak intensity at the beam center. If the total laser power is $p_0$, the normalization condition yields:

$$P_0 = \int_0^\infty I_r 2\pi r dr = \frac{1}{2} I_0 \pi \omega_0^2 \tag{3}$$

This model describes the spatial energy distribution of laser propagation in a homogeneous medium and serves as the initial optical field for subsequent photon tracing.

## 3. Microfacet Statistics and Energy Distribution Model

### 3.1. Absorption–Scattering Attenuation Model in the Seawater Stage

The optical properties of seawater can be divided into two categories: inherent optical properties (IOPs) and apparent optical properties (AOPs). The former are determined solely by the transmission medium itself, whereas the latter depend not only on the medium but also on the surrounding light field [22]. In polar seawater, temperature is an important environmental variable affecting IOPs. The refractive index of seawater depends on wavelength, salinity, and temperature, which can be expressed as $n_{water} = n_{water}(\lambda, S, T)$. The variations in temperature modify the thermal state and density of seawater and consequently change the refractive index. According to radiative transfer theory and the principle of energy conservation, when a laser beam propagates through natural seawater, it passes a differential volume element with cross-sectional area $\Delta V$ and thickness $\Delta r$ [23,24]. The incident laser power generated by the laser source is equal to the sum of the power absorbed by the water, the power scattered by the water, and the power that continues to propagate, as illustrated in Figure 2, which shows the energy distribution of an underwater laser during its transmission through a differential volume element.

$$\Phi_{\mathrm{i}}(\lambda) = \Phi_a(\lambda) + \Phi_s(\lambda) + \Phi_t(\lambda) \tag{4}$$

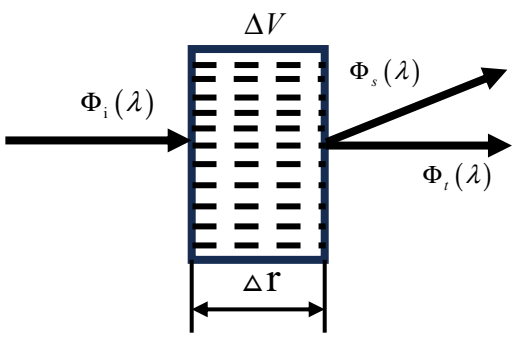


**Figure 2.** The laser passes through a differential volume element.

$\Phi_i(\lambda)$ represents the total incident power, and the components $\Phi_a(\lambda)$, $\Phi_s(\lambda)$, and $\Phi_t(\lambda)$ denote the portions of power lost to absorption, scattering, and unscattered

propagation within the water column. The total attenuation coefficient is defined as $c(\lambda, T) = a(\lambda, T) + b(\lambda, T)$.

Since the sizes of suspended particles and ice crystals in polar under-ice seawater are comparable to the laser wavelength, Mie scattering is the dominant mechanism in the scattering loss. To reduce computational cost while maintaining sufficient accuracy, the Henyey–Greenstein (HG) phase function is adopted to establish the relationship between the scattering angle and a random number, which can be written as [25–27]:

$$\widetilde{\beta}(\lambda) = \frac{1}{4\pi} \frac{1 - g^2}{(1 + g^2 - 2g\cos\theta)^{3/2}} \tag{5}$$

where $\theta$ is the scattering angle, and g is the asymmetry factor. According to the values given earlier, g = 0.95, which indicates that scattering is predominantly in the forward direction and backscattering is relatively weak. The actual scattering direction is determined through random sampling to obtain the stochastic perturbation of the laser propagation direction caused by suspended particles and ice crystals.

### 3.2. Microfacet Statistical Model and Cross-Medium Transmission

Conventional rough-surface optical models mainly focus on reflection or scattering from air–solid or air–water interfaces and are commonly formulated using bidirectional reflectance distribution functions, Kirchhoff approximation, or geometric-optics microfacet theory. Although these models provide useful descriptions of rough-surface scattering, they are not directly tailored to laser transmission across a polar seawater–sea ice interface, where photons have already experienced absorption and multiple scattering in seawater before interacting with the rough ice underside. In natural sea-ice environments, brine drainage-induced pits and channels, ice crystal growth, sea-ice dynamic deformation, and turbulent scouring jointly produce an irregular ice underside. As a result, the water–ice boundary cannot be adequately represented by an ideal planar interface. When the laser beam reaches this boundary, both the local interface geometry and the difference between the refractive indices of seawater and sea ice affect the local incidence angle, Fresnel energy partitioning, and refracted propagation direction, as illustrated in Figure 3.

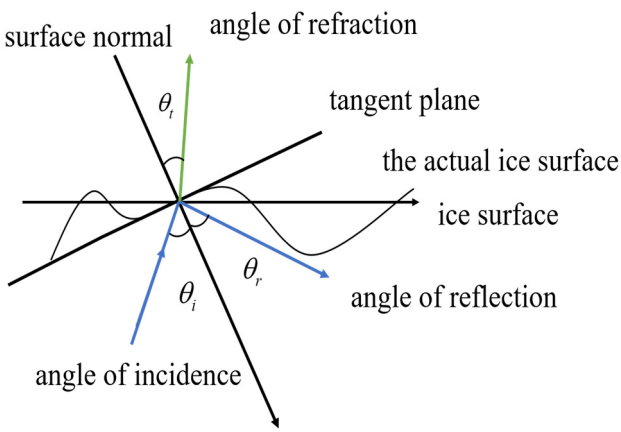


**Figure 3.** Ray paths at a slightly rough water–ice interface.

To account for these effects, the present model integrates underwater absorption–scattering attenuation, microfacet-based statistical roughness, and Fresnel-based cross-medium energy partitioning. The rough water–ice interface is represented as an ensemble of statistically distributed microfacets, as the purpose is not to propose a new microfacet distribution, but to adapt an established statistical rough-surface framework to the cross-medium laser transmission problem at the polar seawater–sea ice interface. In this

framework, the roughness parameter is physically linked to the measurable geometric characteristics of the sea-ice underside, including height variation, spatial correlation, and local surface slope. Therefore, the microfacet model provides a practical way to evaluate how stochastic ice-underside morphology modifies local incidence angle, refraction direction, and transmitted laser energy.

(1) Microfacet Geometric Characterization

The lower surface of sea ice is modeled as a stochastic random surface $z = h(x, y)$, where $h(x, y)$ denotes the height of the ice–water interface relative to the mean interface plane. For a measured or numerically generated ice-underside topography, the RMS height is defined as $\sigma_h = \sqrt{\left\langle \left(h(x,y) - \overline{h}\right)^2 \right\rangle}$, where $\overline{h}$ is the mean interface height and $\langle \cdot \rangle$ denotes spatial averaging. The RMS height $\sigma_h$ describes the vertical amplitude of the ice-underside undulation, whereas the local optical interaction is more directly governed by the surface slope. The local slope components are given by $h_x = \frac{\partial h}{\partial x}, h_y = \frac{\partial h}{\partial y}$; accordingly, the roughness parameter used in the microfacet model is defined as the RMS microfacet slope $\sigma_\beta = \sqrt{\left\langle \left(h^2{}_x - h^2{}_y\right)^2 \right\rangle}$. The local unit normal vector of the surface is expressed as $\overrightarrow{n(x,y)} = \frac{(-h_{x,} - h_{y,} - 1)}{\sqrt{1+h_x^2+h_y^2}}$, where the normal vector is chosen to be directed toward the incident seawater side. The incident photon direction is denoted by $\vec{\mu} = [\mu_x, \mu_y, \mu_z]$, for vertical upward incidence toward the sea-ice underside $\vec{\mu_0} = [0, 0, -1]$. The cosine of the local angle of incidence is then calculated as $\cos\theta_i(x, y) = \left|\vec{\mu_0}, \vec{n}(x, y)\right| = \frac{(\mu_x h_{x,} \mu_y h_{y,} - \mu_z)}{\sqrt{1+h_x^2+h_y^2}}$. Due to the undulation of the macroscopic interface, the normal directions of individual microfacets are randomly oriented, resulting in a statistical dispersion of the incident angle.

(2) Statistical distribution of microfacet slopes

The spatial statistical characteristics of microfacet orientations are governed by the interface roughness parameter. The Beckmann–Gaussian slope distribution is adopted to describe the probability density of the local angle of incidence, $\rho(h_{x,}, h_y) = \frac{1}{\sigma_\beta^2 \pi} exp\left(-\frac{h^2{}_x + h^2{}_y}{\sigma_\beta^2}\right)$, where $\sigma_\beta$ controls the spread of the microfacet slope distribution. Equivalently, since $tan\beta = \sqrt{h^2{}_x + h^2{}_y}$, the slope distribution can be related to the distribution of microfacet tilt angles. The corresponding Beckmann-type angular distribution can be written as $\rho(\theta_i, \sigma_\beta) = \frac{1}{\sigma_\beta^2 \cos\theta_i{}^3} exp\left(-\frac{tan\theta_i{}^2}{\sigma_\beta^2}\right)$, where $\theta_i$ is the local incidence angle determined by the photon direction and the local microfacet normal. The normalization constant is implemented consistently in the Monte Carlo sampling procedure.

The parameter $\sigma_\beta$ provides a direct link between the statistical roughness of the sea-ice underside and the optical transmission model. According to the gradient-based definition given above, $\sigma_\beta$ can, in principle, be calculated from measured ice-underside height fields. In the present study, based on the parameter ranges reported in previous studies, several physically plausible roughness cases are constructed to conduct a sensitivity analysis of cross-medium laser transmission characteristics [28].

(3) Fresnel energy partitioning interface

When a photon interacts with a microfacet, its energy partitioning is determined by the local angle of incidence. Let the refractive index of polar seawater be $n_{water}$ and that of sea ice be $n_{ice}$. The local reflectance for unpolarized light is given by the Fresnel formula $R(\theta_i) = \frac{R_s + R_p}{2}$, where $R_s = \left(\frac{n_{water} cos\ \theta_i - n_{ice} cos\ \theta_t}{n_{water} cos\ \theta_i + n_{ice} cos\ \theta_t}\right)^2$ and $R_p = \left(\frac{n_{water} cos\ \theta_t - n_{ice} cos\ \theta_i}{n_{water} cos\ \theta_t + n_{ice} cos\ \theta_i}\right)^2$. The local transmittance is $T_F(\theta_i)$, satisfying the energy conservation condition $R(\theta_i) + T_F(\theta_i) = 1$.

The corresponding flowchart is presented in Figure 4.

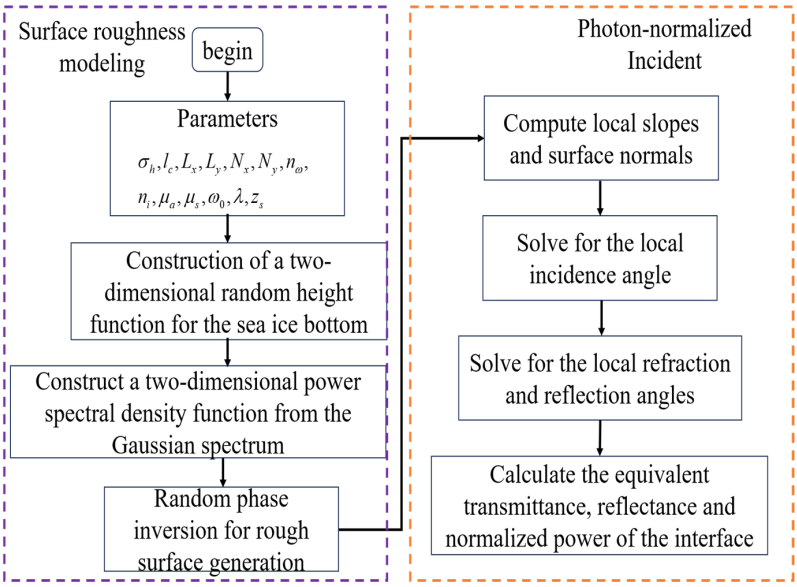


**Figure 4.** Geometric characterization of the interface.

The stochastic rough interface is characterized by the height variation, spatial correlation, and local slope statistics of the ice underside. These geometric quantities are then converted into an equivalent optical roughness description through the microfacet slope parameter $\sigma_\beta$, and the simulation results are presented in Figure 5. This allows the influence of sea-ice underside roughness on incidence-angle broadening, refraction-direction randomization, and Fresnel energy partitioning to be quantified in the Monte Carlo transmission model.

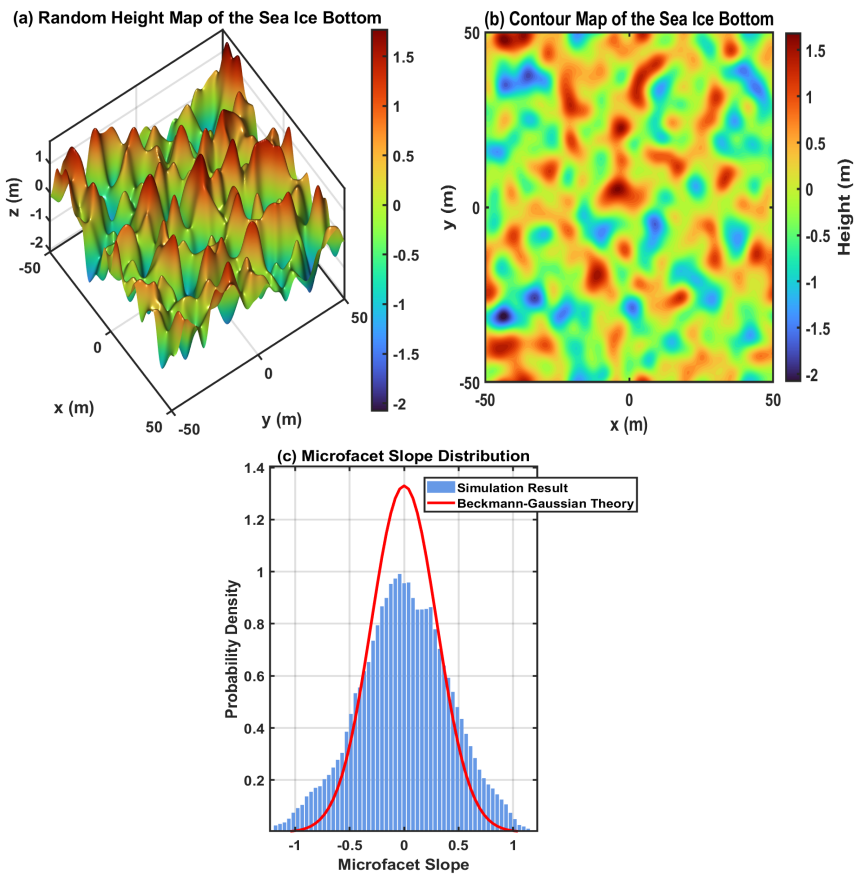


**Figure 5.** Simulated rough morphology of the sea-ice underside.

### 3.3. Cross-Medium Transmission Efficiency and Energy Distribution

To complete the coupled mathematical model for laser transmission through water and ice, the model not only accounts for the attenuation due to absorption and scattering within the seawater medium, but also describes the energy losses arising from local refraction and reflection at the rough water–ice interface. This provides a theoretical reference for the study of underwater cross-medium laser transmission in high-latitude sea regions. The modeling framework is illustrated in Figure 6.

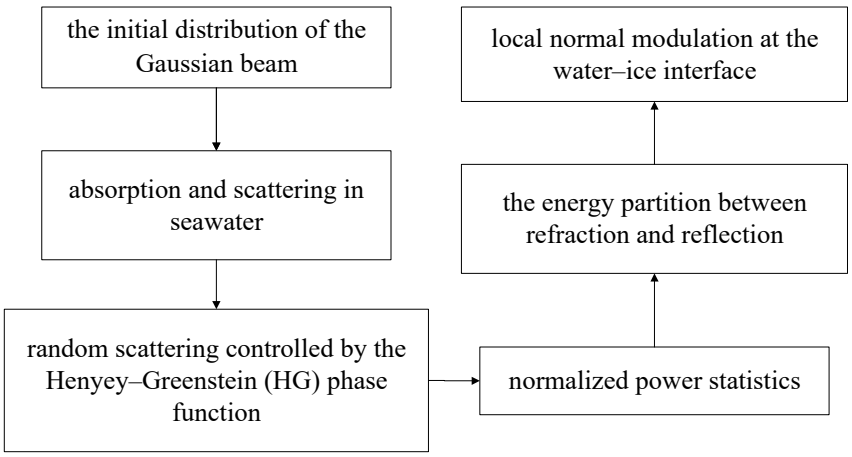


**Figure 6.** Full-process modeling approach.

(1) Monte Carlo Definition of Normalized Power

To quantitatively analyze the energy distribution of the laser after the latter has propagated through seawater to the water–ice interface, normalized power is defined based on Monte Carlo photon weights as follows:

a. Seawater segment transmission. Let the total number of emitted photons be $N_0$ and the sum of photon weights upon arrival at the water–ice interface be $\sum W_k^{int}$. The normalized power at the water–ice interface is defined as $\eta_{int} = \frac{\sum W_k^{int}}{N_0}$, representing the fraction of energy remaining after absorption and scattering in the seawater segment.

b. Sea ice incidence efficiency. Let the sum of photon weights transmitted into the sea ice interior be $\sum W_k^{ice}$. The normalized power entering the sea ice is defined as $\eta_{ice} = \frac{\sum W_k^{ice}}{N_0}$, representing the fraction of energy that enters the sea ice interior after seawater propagation and interface refraction.

c. Interface transmission efficiency. To quantitatively characterize the effect of stochastic undulations at the water–ice interface on the interface transmission efficiency, the latter is defined as $\eta_{tr} = \frac{\eta_{ice}}{\eta_{int}}$, representing the probability that a photon arriving at the interface is successfully transmitted into the sea ice. This metric reflects the combined modulation of interface roughness and azimuthal randomness.

(2) Theoretical Model of Interface Transmittance Efficiency

The local energy distribution at the interface is given by $T_F(x,y) = T_F(\theta_i)$. The normalized power is accordingly expressed as:

$$\overline{T} = \frac{1}{A}\iint_A T_F(\theta_i(x,y))dA = \int_0^{\pi/2} T_F(\theta_i)\cdot\rho(\theta_i,\sigma_h,z_s)d\theta_i \tag{6}$$

The normalized power entering the sea ice interior is defined as:

$$\eta_{ice}(\sigma_h,z_s) = \frac{1}{P_0}\iint_A (E_{\text{int}}(x,y;z_s)T_F(\theta_i(x,y)))dA \tag{7}$$

where $\eta_{ice}$ is the normalized power entering the sea ice, $\sigma_h$ is the root-mean-square roughness of the water–ice interface, $z_s$ is the vertical distance from the laser source to the interface, $P_0$ is the total emitted power, $E_{int}(x, y, z_s)$ is the irradiance distribution at the water–ice interface, $\theta_i(x, y)$ is the local angle of incidence, A is the effective integration area, and the attenuation coefficient is $E_{int}(x, y, z_s) = E_0 e^{-cz_s}$. Equation (8) is derived under the assumptions of homogeneous seawater with constant attenuation coefficient c, elastic photon scattering, a Gaussian transverse beam distribution, and a locally planar Beckmann–Gaussian rough interface. Fresnel coefficients are used for local reflection and transmission, while multiple interfacial reflections and secondary scattering in sea ice are neglected. Combined with the irradiance transfer function, the above equation can be further expressed as:

$$\eta_{ice}(\sigma_h, z_s) = e^{-cz_s} \int_0^{\pi/2} T_F(\theta_i) \cdot \rho(\theta_i, \sigma_h, z_s) d\theta_i \tag{8}$$

It should be noted that Equation (8) represents an effective first-order transmission model rather than a complete radiative-transfer solution for all multiple-scattering and multiple-reflection processes. Equation (8) indicates that, under the above assumptions, two components jointly determine the normalized power entering the sea ice: one $e^{-cz_s}$ is the exponential attenuation caused by absorption and scattering during propagation in seawater, and the additional loss at the rough water–ice interface, which arises from changes in the local incidence-angle distribution that affect transmission across the interface. Therefore, this model provides a unified description of volume transport in seawater and cross-medium transmission at a rough interface, and can be used to quantitatively reveal the coupled influence of seawater optical parameters, propagation distance, and interface roughness on the efficiency of laser energy transmission in high-latitude marine environments.

## 4. Monte Carlo Simulation Model for Laser Transmission

Based on the theoretical model presented in Section 3, a Monte Carlo method is employed to simulate the full-link upward energy transmission process of the laser from the seawater to the water–ice interface [29]. The simulation workflow is illustrated in Figure 7. To improve the efficiency of the numerical implementation, the main input parameters are specified before photon tracing. Photon tracing is divided into four steps: initialization, seawater propagation, rough interface coupling, and statistical output.

(1) Initialization

The water–ice interface is taken as the XOY plane, with the positive $Z$-axis directed vertically downward perpendicular to the interface. The laser source is located at position $z_s$, and the initial photon positions are sampled randomly according to the transverse Gaussian beam distribution. The initial propagation direction is set vertically upward, i.e., $\vec{\mu_0} = [0, 0, -1]$, and the initial photon weight is set to $W_0 = 1$.

(2) Seawater Propagation

The propagation of photons through seawater is simulated by sampling the free-path step length according to the Beer–Lambert law, $S = -ln\zeta/c$, where $\zeta$ is a uniformly distributed random number in (0, 1), and c is the seawater attenuation coefficient. After each step, the photon position and weight are updated. If the photon reaches the water–ice interface, namely $Z \leq 0$, it proceeds to the rough interface coupling stage. The scattering angle and azimuthal angle are sampled using the HG phase function, photon weights are updated according to the attenuation coefficient of seawater, and the azimuthal angle is sampled as $\varphi_s = 2\pi\zeta$. The photon propagation direction is then updated, and photon tracing in seawater is terminated when the photon weight falls below $W_{int}$ or when the scattering number $N_s$ exceeds $N_{max}$.

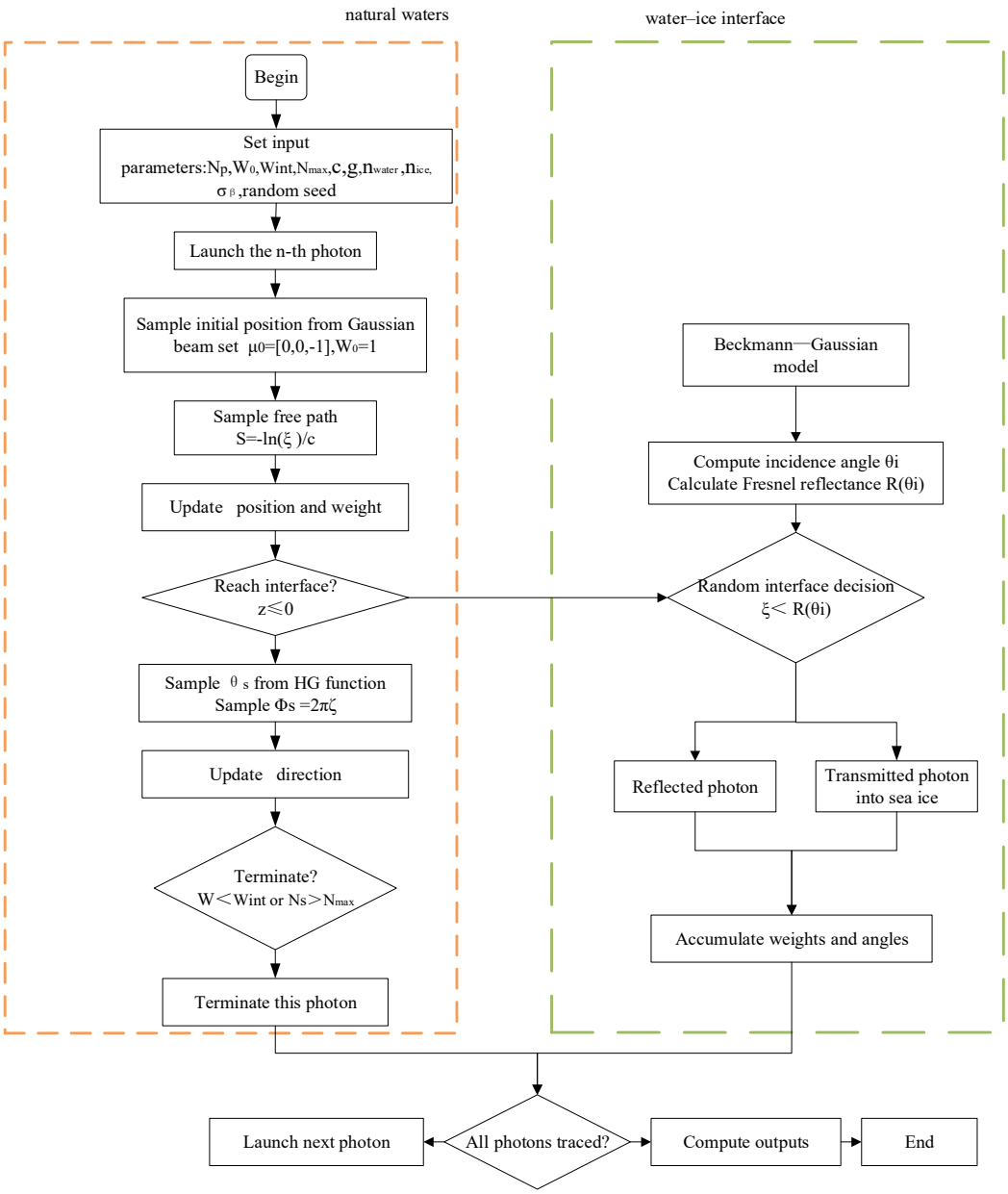


**Figure 7.** Flowchart of the Monte Carlo simulation procedure.

(3) Rough Interface Coupling

When a photon reaches the water–ice interface, the local surface normal is randomly generated according to the Beckmann–Gaussian microfacet model described in Section 3.2. The local incidence angle $\theta_i$ is computed from the photon direction and the local surface normal. The Fresnel reflectance $R(\theta_i)$ is then calculated using the refractive indices of seawater and sea ice. A random number $\zeta_3$ uniformly distributed in (0, 1) is used to determine the photon state at the interface. If $\zeta_3 < R(\theta_i)$, the photon is reflected and remains in the seawater side; otherwise, it is transmitted into the sea ice, and the refraction direction is determined according to Snell's law. The corresponding photon weight, reflection/transmission state, and angular information are recorded for statistical analysis.

(4) Statistical Output

After all $N_p$ photons have been traced, the accumulated photon states are used to calculate the normalized power, the interface transmission efficiency, the incidence-angle and refraction-angle statistics, and the average reflectance and transmission. The normalized power is obtained by summing the corresponding photon weights and normalizing them

by the total launched photon weight. The interface transmittance efficiency is evaluated from the ratio of the photon weight transmitted into sea ice to the photon weight incident on the water–ice interface. The mean, standard deviation, and range of the incidence and refraction angles are also computed from the recorded photon samples. Photon propagation throughout the entire transmission chain is treated as elastic scattering.

## 5. Simulation Results and Analysis

The simulations are carried out using the medium parameters, propagation parameters, and laser source conditions defined in the previous section.

(1) Effect of temperature on the normalized power during seawater propagation

In polar regions, the temperature of seawater beneath sea ice typically ranges from −1.8 °C to 2 °C [30,31]. Temperature variations affect both the concentration and microstructure of ice crystals suspended in seawater. To investigate the influence of temperature on underwater laser propagation, the absorption coefficient, scattering coefficient, and normalized power are calculated for different seawater temperatures, as shown in Figure 8. The simulation results indicate that, when the seawater temperature increases from −1.8 °C to 2 °C, the absorption coefficient increases slightly from 0.0345 to 0.037. This is attributed to the enhanced activity and concentration of impurities in warmer water, which leads to stronger absorption. In contrast, the scattering coefficient decreases from 0.058 to 0.056 with increase in temperature, implying a reduction in the scattering strength. Overall, the attenuation of the laser beam in seawater becomes stronger at higher temperatures. As the temperature rises, the normalized power reaching the water–ice interface exhibits an approximately exponential decrease, indicating increased attenuation during propagation. Consequently, the laser beam transmission performance of seawater is weakened, and the overall energy transmission efficiency of the system is reduced at higher temperatures.

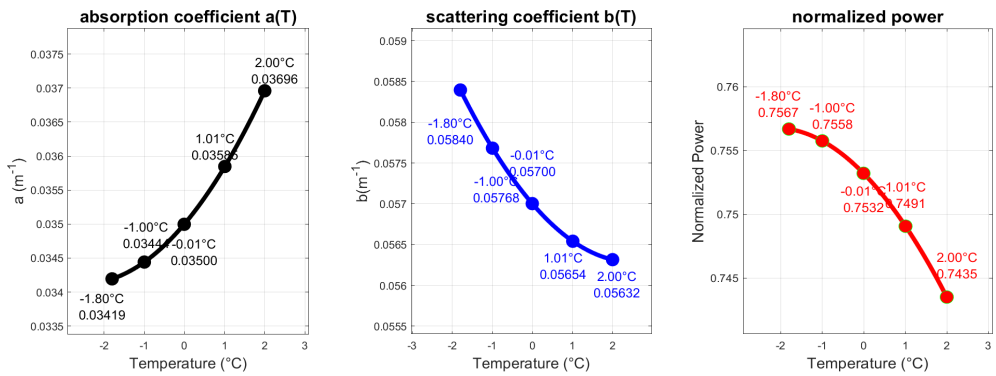


**Figure 8.** Temperature-dependent evolution of Gaussian beam.

(2) Effect of propagation distance on the normalized power in seawater

In a stable temperature environment, the distance between the laser source and the underside of the sea ice is varied so that the underwater propagation distance changes from 2 m to 0 m (the coordinate origin is located at the water–ice interface, and the positive *Z*-axis points downward). The variations in beam waist radius, spot shape, and normalized power of the Gaussian beam at different propagation distances are analyzed, as shown in Figure 9. The simulation results show that, as the distance between the laser emitting device and the water–ice interface decreases from 2 m to 0 m, the beam waist radius increases with propagation distance, and the spot size at the interface gradually increases. On the other hand, the normalized power exhibits an overall exponential decay with distance. Due to the relatively short propagation range and the small optical attenuation coefficient in polar seawater, this exponential decay appears approximately linear over the

considered distances. These results indicate that the photon energy decays exponentially with propagation distance: long-distance transmission leads to stronger beam divergence and reduced power density, whereas at shorter distances the beam remains more tightly focused and achieves a higher energy transmittance through the interface.

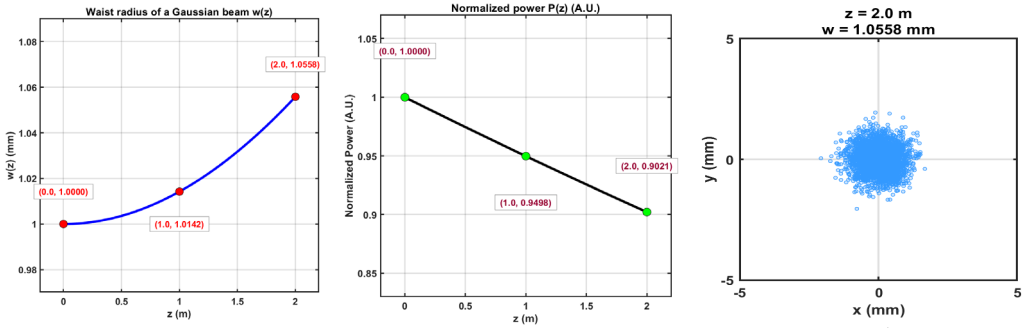


(**a**) Beam waist radius (**b**) Normalized power (**c**) Spot shape

**Figure 9.** Evolution of the Gaussian beam with propagation distance in seawater.

(3) Effect of water–ice interface topography on the normalized power during interface transmission

A small-scale roughness model of the ice interface is developed based on the optical parameters of seawater and sea ice in polar environments, and the random variation in the sea ice bottom topography modelled using a Gaussian spectral method. By varying the surface roughness of the sea ice, the influence of local slope on the incident angle distribution of underwater laser propagation at the water–ice interface is investigated, as well as the corresponding transient power incident onto the interface, The simulation results are illustrated in Figure 10. The simulation results indicate that when the interface slope is small (close to a flat surface), the photon incident angles mainly concentrate within the laser divergence angle range of approximately 5° to 15°. As the local slope increases to a range between 0.3 and 0.45, the incident angles $\theta_i$ rapidly increase to between 20° and 35°. This demonstrates that greater undulations or steeper slopes in the sea ice bottom cause stronger deviations between the light rays and the local interface normal vector, resulting in a broadened incident angle distribution. Under polar conditions, the refractive indices of seawater and ice are very similar; thus, when the incident angle is below 20°, the transmission coefficient remains nearly constant and approaches 100%. This implies negligible reflection loss at the ice interface, and laser attenuation due to interface reflection can be ignored. However, as the incident angle increases from 20° to 30°, the transmission decreases sharply. Beyond 30°, the reflectance rises rapidly, leading to a significant reduction in laser power transmitted through the sea ice. Overall, due to the combined effects of rough interface normal vector deviation and scattering in seawater, the incident angle distribution broadens significantly. Increasing interface roughness results in larger incident angles of photons arriving at the interface, extending the range from near 0° to about 30°. The enhanced roughness causes energy to scatter in multiple directions and disperses the transmitted laser beam. These findings demonstrate that microtopographic variations in the sea ice bottom surface have a pronounced impact on the coupling efficiency of laser transmission at the water–ice interface in polar regions.

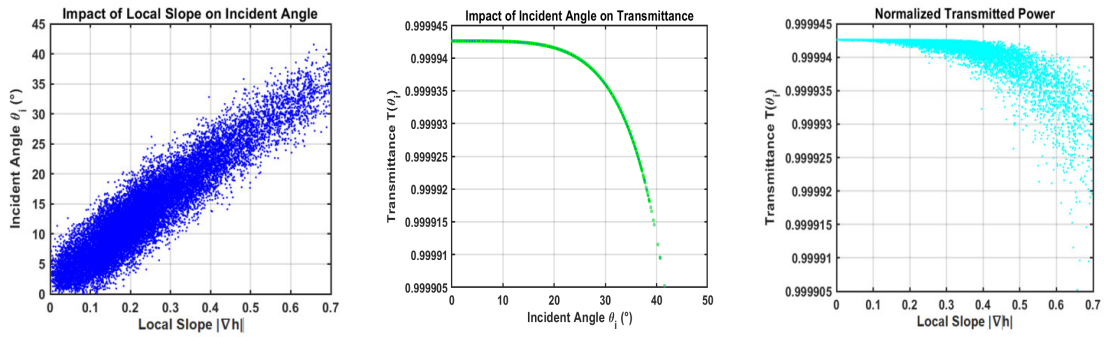


(**a**) Refraction angle distribution (**b**) Transmittance (**c**) Normalized power

**Figure 10.** Effect of sea underside topography on Gaussian beam propagation.

## 6. Experimental Validation

The underwater laser lidar used in the experiment is an integrated and sealed measurement unit. The laser transmitter, receiving module, measurement software, and preliminary data processing system are packaged inside a black housing unit, as shown in Figure 11. The host computer is used to control the lidar unit and record the output signal from the built-in acquisition and processing system. Since the optical transmitter, receiver, and internal processing module are integrated within the sealed device, the validation in this study is conducted at the system-output level. Therefore, we analyze repeatability and statistical variation in the measured output signal under controlled experimental conditions, rather than separately calibrating each internal component. For each experimental condition, repeated measurements are performed while maintaining the same system settings, including laser operating mode, receiver gain, sampling configuration, and data processing parameters. The background level is estimated from the baseline of the acquired waveform, and the echo signal intensity is calculated from the difference between the echo peak and the baseline level. The measured signal intensity is used as a relative indicator of the received laser energy. The mean value and standard deviation are reported.

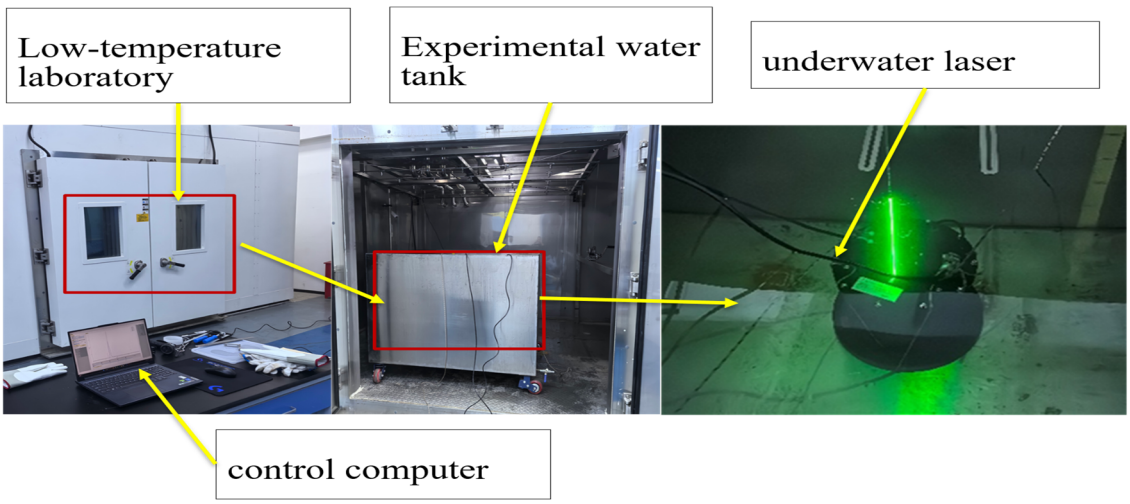


**Figure 11.** Experimental environment and underwater laser.

The main uncertainty sources include laser pulse fluctuation, receiver response fluctuation, the internal signal processing of the integrated lidar unit, water-temperature control accuracy, water-depth adjustment error, relative positioning error between the lidar and the ice sample, salinity variation, and nonuniformity of the ice surface. Because the lidar system

is sealed and integrated, these uncertainty factors are evaluated through the statistical dispersion of the system-level output signals obtained from repeated measurements.

Experiment 1 is conducted with an ice layer thickness of 50 mm and a salinity of 35‰, and the water depth is set to 0.5 m. Under these conditions, the energy of the laser beam reaching the water–ice interface is measured at two temperature values: a room-temperature environment of 17 °C and a low-temperature environment of 0 °C. The measurement results are shown in Figure 12.

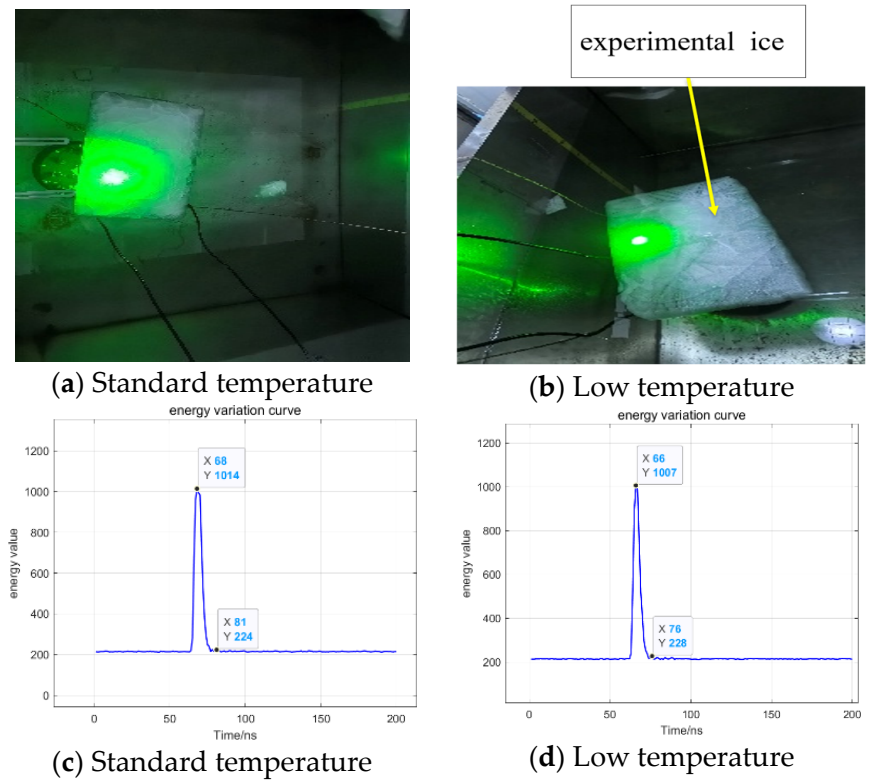


**Figure 12.** Data acquisition.

By processing the acquired echo signals, as shown in Figure 12, the energy loss is 790 μJ under normal temperature conditions and 779 μJ under low-temperature conditions. This agrees with the simulation results, which indicate that energy loss increases with the rise in temperature.

In Experiment 2, the ice layer thickness is set to 50 mm, and the salinity is 35‰. Under these experimental conditions, the energy of the laser beam reaching the water–ice interface is measured for two values of water depth at which the laser source is positioned is varied. The measurement results are shown in Figure 13.

Laser energy measurements are conducted at different distances based on the processing of the collected echo signals, as shown in Figure 13. When the water depth is 50 cm, the echo energy loss after reflection from the sea ice is measured to be 735 μJ, while at a water depth of 75 cm, the echo energy loss increases to 776 μJ. This trend aligns with the simulation results, confirming that energy loss increases with propagation distance.

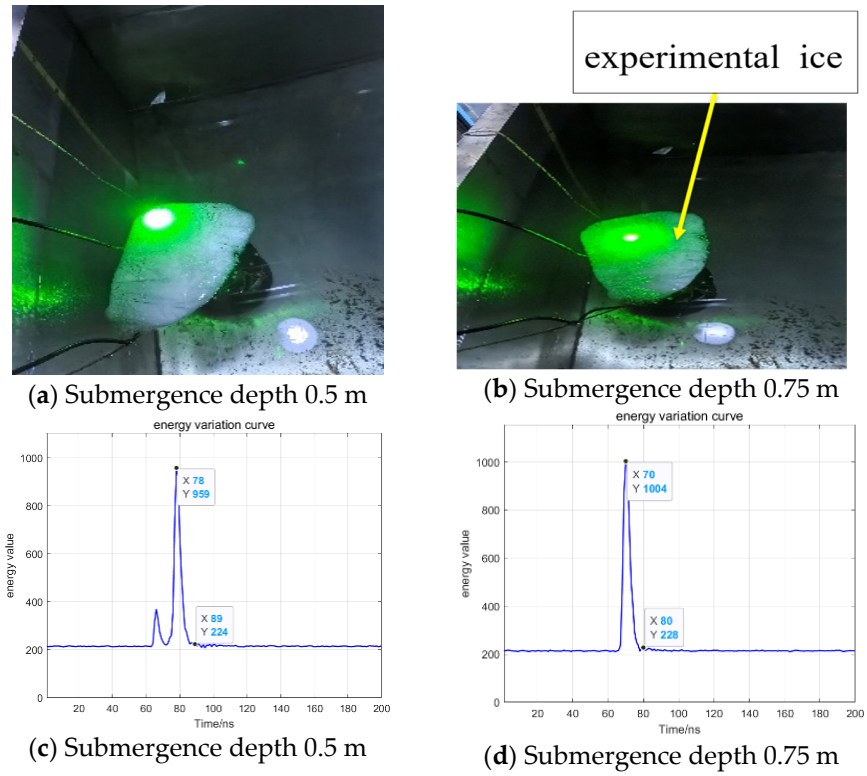


**Figure 13.** Experiments at different depths.

## 7. Conclusions

Against the background of cross-medium upward wireless energy transmission applications of underwater lidar in polar environments, experimental and simulation results are compared. It is found that the simulation results are close to the experimental results, fully demonstrating the effectiveness of the model and the correctness of the simulation. Collectively, the research results show following:

(1) When laser propagates in natural polar water, increasing the temperature reduces the laser's penetration capability.

(2) Reducing the distance between the laser source and the water–ice interface makes the energy more concentrated, and the normalized power reaching the interface increases linearly.

(3) When the laser passes through the water–ice interface, the laser transmission efficiency decreases rapidly when the incident angle exceeds 30°. Therefore, the smoother the ice surface, the better the laser penetration and the weaker the reflection is.

Overall, the findings of this study can provide a reference for selecting underwater laser detection application scenarios in polar environments, as well as for sea ice detection and efficiency evaluation. This employs the principles of geometric optics. However, laser energy suffers severe attenuation underwater, which is unfavorable for investigating laser transmission inside ice. Therefore, subsequent research will focus on the study and analysis of polarization optics.

**Author Contributions:** Z.W. was responsible for the conceptualization, overall framework construction, and full-text writing of the manuscript; W.G. undertook the formal analysis of data, model validation, and result verification; X.L. was in charge of fund acquisition and budget coordination for the research project; L.Y. and X.X. jointly completed the collection, sorting, checking, and standardization of data; S.Z. carried out relevant investigation work and collected basic materials and experimental data required for the research; Z.S. was responsible for the construction, optimization, and technical route design of the research methodology; J.H. provided experimental resources, equip-

ment support, and relevant technical guarantees required for the research. All authors have read and agreed to the published version of the manuscript.

**Funding:** This work was supported by the Hubei Provincial Natural Science Foundation of China (Grant No. 2026AFD089).

**Institutional Review Board Statement:** Not applicable.

**Informed Consent Statement:** Not applicable.

**Data Availability Statement:** The data sets used and/or analyzed during the current study are available from the corresponding author upon reasonable request.

**Acknowledgments:** We acknowledge the support provided to this study by the Naval University of Engineering in the form of time availability and facilities.

**Conflicts of Interest:** The authors declare no conflicts of interest.

## References

1. Liu, J.P.; Wang, S.Y.; Song, M.R. Rapid changes in polar sea ice and advances and challenges in mechanism research. *Acta Meteorol. Sin.* **2025**, *83*, 676–698.
2. Han, X.T.; Liao, P.X.; Li, P. Monte Carlo simulation of laser transmission characteristics in underwater channels. *Opt. Commun. Res.* **2023**, *49*, 53–59.
3. Moore, K.D.; Jaffe, J.S.; Ochoa, B.L. Development of a new underwater bathymetric laser imaging system: L-bath. *J. Atmos. Ocean. Technol.* **2000**, *17*, 1106–1117. [CrossRef]
4. Egerev, S.V.; Fokin, A.V. Laser-induced cavitation: Statistics, Monte Carlo modeling, and experiments. *J. Atmos. Ocean. Technol.* **2000**, *17*, 1106–1117.
5. He, J.H.; Duan, J.; Zhan, J.T. Analysis of the influence of underwater medium concentration on laser polarization transmission characteristics. *Laser Optoelectron. Prog.* **2021**, *58*, 302–309. [CrossRef]
6. He, Y.; Liu, Y.; Liu, C. Analysis of transmission depth and photon number in Monte Carlo simulation for underwater laser transmission. *Remote Sens.* **2022**, *14*, 2565. [CrossRef]
7. Guo, S.; He, Y.; Chen, Y.; Chen, W.; Chen, Q.; Huang, Y. Monte Carlo simulation with experimental research about underwater transmission and imaging of laser. *Appl. Sci.* **2022**, *12*, 8959. [CrossRef]
8. Ren, Y.R.; Zong, S.G.; Liang, S.Y. Research on transmission characteristics of blue-green laser communication under complex water quality conditions. *Laser Infrared* **2023**, *53*, 355–361.
9. Yu, W.C. Simulation and Energy-Transfer Experiments of Laser Transmission in the Marine Environment. Master's Thesis, Chongqing University, Chongqing, China, 2024. [CrossRef]
10. Gao, P.; Li, B.; Dong, S.; Yuan, Y. Analysis of the Echo Characteristics of Pulsed Laser Detection of Underwater Targets. *J. Eng. Thermophys.* **2023**, *44*, 1698–1703.
11. Huang, A. Underwater Laser Communication Channel Characteristics Based on Monte Carlo Simulation. *Infrared Laser Eng.* **2017**, *46*, 226–231. [CrossRef]
12. Beckmann, P. II Scattering of light by rough surfaces. In *Progress in Optics*; Elsevier: Amsterdam, The Netherlands, 1967; Volume 6, pp. 53–69.
13. Zhang, Y.; Zhong, Z.; Zhang, B. Generalized Beckmann-Kirchhoff scattering model for ultra-smooth surfaces. *J. Mod. Opt.* **2025**, *72*, 228–239. [CrossRef]
14. Chen, H.; Hu, Y.Z.; Wang, H.; Wang, W.Z. Simulation and Characterization of Fractal Features of Rough Surfaces. *J. Mech. Eng.* **2006**, *42*, 219–223. [CrossRef]
15. Welton, P.J. Comparison of slope approximations used in rough surface scattering. *J. Acoust. Soc. Am.* **2015**, *137*, EL220–EL225. [CrossRef] [PubMed]
16. Zhao, M.W.; Wang, W.G.; Fang, J.Y. Distribution of suspended matter content and its particle composition characteristics in the northern Bering Sea. *Acta Oceanol. Sin.* **2016**, *38*, 82–93.
17. Zhang, X.Z.; Zhai, M.S.; Zhou, L.J. Influence of sea ice on underwater quantum communication channel performance. *Acta Opt. Sin.* **2023**, *43*, 132–138.
18. Quan, X.; Fry, E.S. Empirical equation for the index of refraction of seawater. *Appl. Opt.* **1995**, *34*, 3477–3480. [CrossRef] [PubMed]
19. Perovich, D.K. *Optical Properties of Sea Ice*; CRREL: Hanover, NH, USA, 1996.
20. Cai, Q. Research on Ice Thickness Measurement Technology Based on Raman Spectroscopy Identification. Master's Thesis, Harbin Engineering University, Harbin, China, 2020.

21. Warren, S.G. Optical properties of ice and snow. *Philos. Trans. R. Soc. A Math. Phys. Eng. Sci.* **2019**, *377*, 20180161. [CrossRef] [PubMed]
22. Cha, B. Research on Underwater Synchronous Scanning All-Round Laser Near-Range Target Detection. Ph.D. Thesis, Nanjing University of Science and Technology, Nanjing, China, 2015.
23. Zaneveld, J.R.V. Light and Water. In *Radiative Transfer in Natural Waters*; Academic Press: Cambridge, MA, USA, 1995.
24. Perovich, D.K.; Roesler, C.S.; Pegau, W.S. Variability in Arctic sea ice optical properties. *J. Geophys. Res. Ocean.* **1998**, *103*, 1193–1208. [CrossRef]
25. Morel, A. *Volume Scattering Function of Selected Oceanic Waters*; UNESCO Technical Papers in Marine Science; Academic Press: Cambridge, MA, USA, 1972.
26. Gui, D.; Meng, H.R.; Yang, H. Numerical simulation of propagation characteristics of Gaussian laser beam in seawater based on Mie scattering model. *Laser Optoelectron. Prog.* **2024**, *61*, 168–176.
27. Fofonoff, N.P.; Millard, R.C. *Algorithms for Computation of Fundamental Properties of Seawater*; UNESCO Technical Papers in Marine Science; UNESCO: Paris, France, 1983.
28. Bian, X.; Shao, Y.; Tian, W.; Wang, S.; Zhang, C.; Wang, X.; Zhang, Z. Underwater topography detection in coastal areas using fully polarimetric SAR data. *Remote Sens.* **2017**, *9*, 560. [CrossRef]
29. Petty, A.A.; Kurtz, N.T.; Kwok, R.; Markus, T.; Neumann, T.A. Winter Arctic sea ice thickness from ICESat-2 freeboards. *J. Geophys. Res. Ocean.* **2020**, *125*, e2019JC015764. [CrossRef]
30. Liu, H.; Ji, H.L.; Luo, H.C. Application of UAV-borne radar in ice thickness and ice layer structure detection. *J. Drain. Irrig. Mach. Eng.* **2021**, *39*, 630–636.
31. Li, W.; Hsu, C.Y.; Tedesco, M. Advancing Arctic sea ice remote sensing with AI and deep learning: Opportunities and challenges. *Remote Sens.* **2024**, *16*, 3764. [CrossRef]


**Disclaimer/Publisher's Note:** The statements, opinions and data contained in all publications are solely those of the individual author(s) and contributor(s) and not of MDPI and/or the editor(s). MDPI and/or the editor(s) disclaim responsibility for any injury to people or property resulting from any ideas, methods, instructions or products referred to in the content.